Colloids and Surfaces A: Physicochemical and Engineering Aspects 675 (2023) 132040

Contents lists available at ScienceDirect

Colloids and Surfaces A: Physicochemical and Engineering Aspects

journal homepage: www.elsevier.com/locate/colsurfa

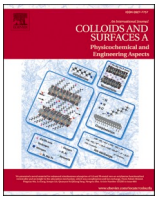

Enhancing corrosion resistance of anodized AA7075 alloys by electrodeposition of superhydrophobic coatings

Vincenzo Verro, Francesco Di Franco *, Andrea Zaffora, Monica Santamaria

Università degli Studi di Palermo, Dipartimento di Ingegneria, Viale delle Scienze, Ed. 6, 90128 Palermo, Italy

GRAPHICAL ABSTRACT

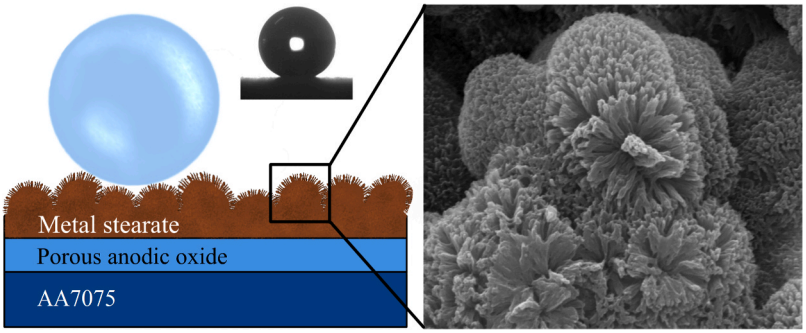

ARTICLE INFO

Keywords:
AA7075
Anodizing
Superhydrophobic coatings
Electrodeposition
Stearate
Contact angle

ABSTRACT

Electrodeposition of superhydrophobic coatings was carried out on anodized AA7075 alloy to further enhance its corrosion resistance. Several compositions of electrodeposition bath were studied to find the most suitable one to obtain superhydrophobic coating. Scanning Electron Microscopy and Fourier Transform Infrared Spectroscopy proved the deposition of coatings with different characteristics depending on electrodeposition bath composition. Highest contact angle value (~ 160°) and highest corrosion resistance were obtained for the Mn-containing coating, proving also high stability after 21 days of immersion in an aqueous solution mimicking seawater. Experiments on flat pellet samples were carried out to split the effect due to the material composition with respect to that due to the coating morphological features, estimating the vacuum fraction of the superhydrophobic coatings according to the Cassie Baxter model.

1. Introduction

Aluminium alloys AA7075 are widely used in aerospace, defence and automotive industries due to their superior mechanical properties, resistance to fatigue and high strength to weight ratio. The latter can be reached by alloying aluminium with other elements such as copper, magnesium, silicon, manganese, and zinc that is the main alloying element. However, AA7075 has poor corrosion resistance due to the resulting alloy microstructure containing intermetallic particles that, being more or less noble than the alloy matrix, increase the corrosion susceptibility of the alloy compared to pure aluminium [1,2]. To enhance corrosion protection and, at the same time, to improve

* Corresponding author.
E-mail address: francesco.difranco@unipa.it (F. Di Franco).

https://doi.org/10.1016/j.colsurfa.2023.132040
Received 6 July 2023; Accepted 9 July 2023
Available online 13 July 2023

adhesion with paint, AA7075 are typically anodized in a chromic acid bath to induce a self-healing action thanks to the residual chromate ions presence inside the pores of the anodic layer. Environmental concerns and legal restrictions induced to replace the chromic acid bath with other electrolytes and, among them, tartaric acid/sulphuric acid (TSA)-based solutions resulted to provide a good corrosion resistance. This can be further enhanced by a hot water treatment in order to seal the pores of the anodic oxide [3].

Another strategy able to improve corrosion resistance of aluminium alloys is to make their surface superhydrophobic to hinder the contact with water or moisture and, simultaneously, to provide self-cleaning and anti-icing properties [4]. Surface wettability can be assessed by measuring the value of the contact angle, which is defined as the angle between the solid surface and the tangent to the liquid–vapor interface that is formed at the three-phase contact line [5]. When a static contact angle exceeds 150°, the solid surface can be defined as super-hydrophobic. The surface wettability depends on both the surface layer composition and on its roughness, and there are several models to explain such dependence. Wenzel model [6] describes contact angle of fully wetted surface with dependence on surface roughness, while Cassie-Baxter model [6] accounts for the presence of air pockets entrapped inside the available space between surface asperities and thus laying below liquid droplet, and describes the interface between solid and liquid.

Many techniques were studied to synthesize superhydrophobic coatings to enhance corrosion resistance of Al and Al alloys [7–11]. Anyway, often these treatments are not easily implementable in the typical Al industrial processes. In this context, it was successfully demonstrated that the corrosion resistance of AA5083 can be enhanced by a synergistic action between anodic films and superhydrophobic layers grown by electrodepositing a manganese stearate layer on top of porous alumina [12]. The electrodeposition process is very sensitive to the features of the anodic films, since the conductivity of barrier layer as well as pores' diameter and length can influence the thickness, uniformity and morphology of the layer responsible of super-hydrophobicity.

In this work we want to test a strategy to carry out an electrodeposition process aimed to induce the precipitation of different metal stearates, trying to make the surface of anodized AA7075 super-hydrophobic and in the meantime seal the pores of the anodic layer grown in TSA electrolyte. The effect of this surface treatment on the corrosion resistance of the alloy in aggressive environment will be assessed by electrochemical measurements. To adequately characterize the wettability of the surfaces, static contact angles as well as receding and advancing contact angles of the liquid on the substrate will be measured.

2. Materials and methods

2.1. Preparation of samples

Specimens of the AA7075 alloy (0.4 wt% Si, 0.5 wt% Fe, 0.3 wt% Mn, 2.1–2.9 wt% Mg, 1.2–2.0 wt% Cu, 5.1–6.1 wt% Zn, 0.18–0.28 wt% Cr, 0.20 wt% Ti, Al balance) were initially mechanically treated with abrasive papers (P500, P800, P1200) and then ultrasonically cleaned in acetone for 15 min, and in distilled water for 5 min. After that, samples were chemically treated in aqueous solution with 10 wt% NaOH, at 60 °C for 30 s. Then, they were immersed in 30 vol% HNO_3 aqueous solution for 15 s. The described processes are known as alkaline etching and desmutting respectively, and they are usually used to remove passive film that may form at the surface of aluminium exposed to air and to remove possible intermetallic particles from the surface. After each described process, specimens were rinsed in distilled water.

2.2. Anodizing process

The formation of the anodic film on the samples was performed in TSA (tartaric sulfuric acid). TSA was prepared as an aqueous solution with 0.46 M sulfuric acid (H_2SO_4) and 80 g l^{-1} of tartaric acid ($C_4H_6O_6$). Anodizing was performed at 37 °C, potentiostatically at 14 V, with a moderate stirring action. In the two-electrode configuration used in this work, Al alloy sample was the working electrode whilst an aluminium 99.9999% pure foil was used as the cathode (counter electrode).

2.3. Pore sealing

To make a comparison with electrodeposition sealing process, porous anodic layer was also sealed by means of the hot water sealing procedure: these samples (HWS) were immersed in deionized water at 96 °C for 30 min, in order to hydrate Al_2O_3 anodic film with a subsequent increase in volume. After that, samples were dried at room temperature.

2.4. Deposition of the coating

Electrodeposition solution was prepared using dimethylsulphoxide (DMSO, $(CH_3)_2SO$) as the solvent and stearic acid ($CH_3(CH_2)_{16}COOH$) 0.1 M as fatty acid, maintaining a constant temperature of 50 °C and a stirring action for 20 min. Four different solutions were investigated with compositions listed in Table 1.

The electrodeposition procedure was carried out with a two-electrode configuration potentiostatically at − 30 V without stirring action, maintaining a 50 °C constant temperature, with two sheets of carbon paper used as anodes. In order to have a coating adherent to the substrate the deposition lasted for 3 min, since longer time and thus circulated charge caused the formation of thick powdered layers. After that, samples were rinsed in ethanol and dried for 24 h at room temperature.

2.5. Pellets preparation

To prepare pellets of coating material, a pelletizing process was used. In details, coating powder was obtained by scraping the coatings from the substrate after electrodeposition process. Coating powder was then pressed with 10 tons for 10 s by using a Pellet press (C-30 Compression Tester, Riic London, England Lab Scientific). Pellets were prepared to have a flat surface in order to evaluate coating wettability not affected by roughness.

2.6. Samples characterization

Surface morphology of the specimens was analysed using a FEI Quanta 200 FEG SEM instrument, combined with a X-ray energy dispersive (EDX) system. Beforehand, on each sample was deposited a thin Au layer by sputtering. Fourier Transform Spectroscopy in the range 4000 – 450 cm^{-1} was adopted to analyse the composition of the coating, using a FT-IR/NIR Spectrum 400 spectrophotometer (PerkinElmer, Waltham, MA, U.S.A.). Measurement of contact angle was carried out with an FTA 1000 instrument, analysing droplets of 5 μl of deionized water and toluene. For the determination of water contact angle hysteresis, dynamic contact angles were measured: advancing angle was

Table 1
Different solutions used for the electrodeposition processes. Solvent: DMSO.

	Fatty acid	Metallic Salt		
1. Mn coating	stearic acid 0.1 M	manganese (II) chloride tetrahydrate	$MnCl_2$ 4 H_2O	0.05 M
2. Na coating	stearic acid 0.1 M	sodium chloride	NaCl	0.05 M
3. Sn coating	stearic acid 0.1 M	tin (II) chloride dihydrate	$SnCl_2$ 2 H_2O	0.05 M
4. Zn coating	stearic acid 0.1 M	zinc (II) chloride	$ZnCl_2$	0.05 M

measured by a linear increase in droplet volume, from 5 μl to 25 μl during a 200 s acquisition time. Receding angle was obtained similarly, acquiring images during a linear reduction of the volume from 25 μl to 5 μl. Every value was averaged at least on 3 different measurements.

The surface free energies of the metal stearates were calculated with the OWRK method [13] with water and toluene as the testing liquids.

2.7. Electrochemical measurements

Electrochemical behaviour of the samples was evaluated in 3.5 wt% NaCl aqueous solution to mimic an aggressive environment for aluminium, such as seawater. For every specimen corrosion potential, E_{corr}, was measured as the Open Circuit Potential (OCP) after a 3600 s stabilization time. Impedance spectra were collected at the E_{corr} with an ac signal of 10 mV amplitude in the frequency range 10 mHz – 100 kHz. Specimens were studied as the working electrode in a three-electrode configuration, with a Pt electrode as the counter and an Ag/AgCl/sat. KCl reference electrode (0.197 V vs SHE). All the experimental data were collected with a PARstat 2273 and impedance spectra were then fitted with the software ZSimpWin.

3. Results and discussion

3.1. Anodizing and electrodeposition processes

Anodizing of the samples was carried out in TSA operating potentiostatically at 14 V for 20 min, maintaining a 37 °C constant temperature and a moderate stirring. Fig. 1 shows the growth curve associated to the described anodizing process.

At the beginning of the anodizing process (almost 190 s) the measured current raises indicating the formation of the barrier-type anodic layer. After this first growth phase, the current decreases reaching (after 600 s) an almost constant value of ~ 9 mA cm^{-2}. This plateau could be related to the thickening of the porous layer [14].

Electrodeposition of the coating is induced polarizing cathodically the anodized AA7075 samples in DMSO solution containing stearic acid and the selected metal salt (see experimental section) in order to obtain a hybrid organic/inorganic coating. The current transients recorded during the potentiostatic polarization at − 30 V are reported in Fig. 2.

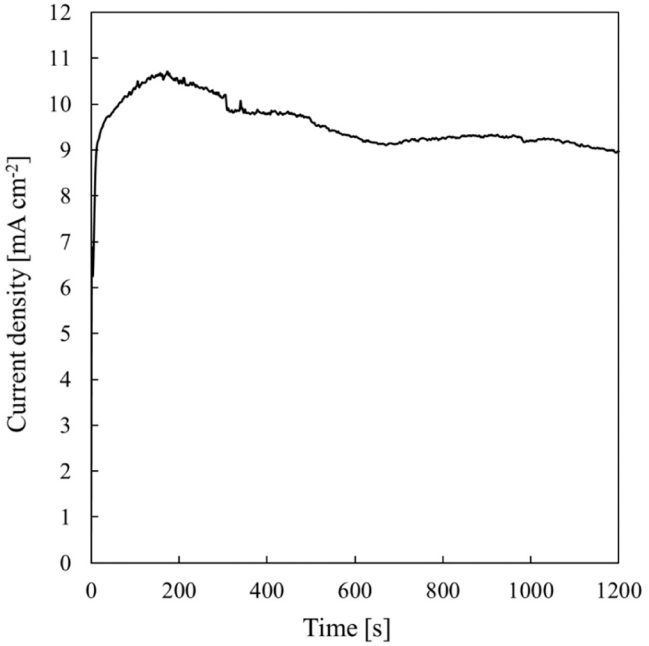

Fig. 1. Current density vs time during anodizing in TSA bath.

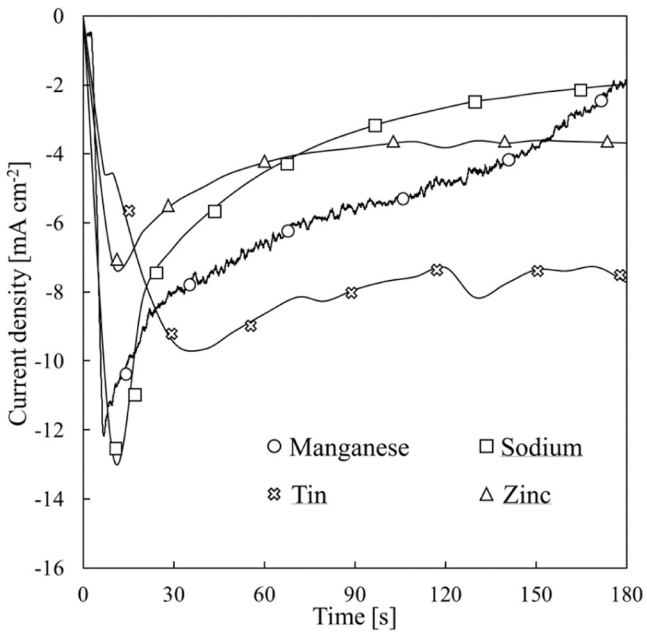

Fig. 2. Current density vs time curve recorded during the electrodeposition process carried out at - 30 V.

The imposed voltage mainly drops inside the barrier layer beneath the porous layer grown by anodizing. Indeed, anodic alumina is an insulating material and a strong potential difference is necessary to allow the circulation of an electronic current. The latter is responsible of reduction processes involving hydrogen ions produced by stearic acid dissociation according to the following reactions:

$$CH_3(CH_2)_{16}COOH \leftrightarrow CH_3(CH_2)_{16}COO^- + H^+ \quad (1)$$

$$2\,H^+ + 2e^- \rightarrow H_2\uparrow \quad (2)$$

The reduction of the protons leads to a shifting in the equilibrium of the reaction (1) toward the formation of stearate ions, promoting the coating growth [12]. The increased concentration of stearate ions induces the precipitation of the metal salt according to the following reaction:

$$M^{z+} + zCH_3(CH_2)_{16}COO^- \rightarrow M[CH_3(CH_2)_{16}COO]_z\downarrow \quad (3)$$

The stearic acid is a fatty acid with a long carbon chain, and it is responsible for the hydrophobic behaviour of the coating [15]. The successful precipitation of metal stearates was confirmed by SEM microscopy, while their composition was studied by EDX and FTIR. Table 2 reports the percentages of the elements revealed by EDX in the coatings. The high percentages of C and metal related to the cations present in the electrodeposition bath, confirm an effective deposition of the metal stearate, as described in ref. [12].

Table 2
Chemical composition of the coatings.

Mn coating	**C K**	**O K**	**Al K**	**Mn K**	**Total**
wt%	76.3	11.66	0.19	11.86	100.00
at%	86.97	9.98	0.1	2.96	100.00
Na coating	**C K**	**O K**	**Al K**	**Na K**	**Total**
wt%	77.86	11.91	1.54	8.69	100.00
at%	84.61	9.72	0.74	4.93	100.00
Sn coating	**C K**	**O K**	**Al K**	**Sn K**	**Total**
wt%	52.37	10.01	0.70	36.92	100.00
at%	81.91	11.75	0.49	5.84	100.00
Zn coating	**C K**	**O K**	**Al K**	**Zn K**	**Total**
wt%	77.50	9.51	0.04	12.95	100.00
at%	89.04	8.21	0.02	2.73	100.00

FT-IR spectra recorded for all the coatings are reported in Fig. 3a)-d). For all electrodeposited coatings, absorption bands in the range 2912–2916 cm^{-1} and 2847–2451 cm^{-1} can be seen in the FT-IR spectra; these can be attributed to -CH- asymmetric and symmetric vibrations, respectively [16]. Multiple bands in the range 1398–1562 cm^{-1} appear and can be attributed to the $-COO^-$ moieties due to the formation of a stearate salt.

3.2. Morphology and wettability

SEM images of coated samples are shown in Fig. 4a)-d). In Fig. 4a it can be seen the presence of cauliflower-like formations in the coating containing the Mn salt. Due to the incremental growth of the coating obtained with the electrodeposition process, micrometric structures with nanometric extremities assemble together to create hierarchical structures, in agreement with previous experimental findings on AA5083 alloy [12]. For the coating obtained with Zn salt (see Fig. 4b) the hierarchical structure is less pronounced but still present. The coatings containing Sn and Na salt show different morphologies (see Figs. 4c and 4d).

Fig. S1 shows the surfaces of the metal stearate pellets (see experimental section). It can be seen that all the pellets' surfaces appear flat even at high magnification. EDX analysis for coatings and pellets confirmed the presence of C, O and the corresponding metal in agreement with the results of FT-IR.

In order to assess the water wettability of the coating, static contact angle, θ, as well as contact angle hysteresis (the difference between advancing angle, θ_{adv}, and the receding angle, θ_{rec}) were measured. Figs. 5 and 6 report the values of the static contact angles and contact angle hysteresis, obtained for the pellets and for the coatings respectively, as well as those measured on the HWS samples.

For the pellets, the static contact angles for Mn, Sn and Zn stearates were between 100° and 105°, thus suggesting that those stearate-containing powders are hydrophobic. The Na stearate pellet showed different behaviour, with static contact angle measured of ~ 74°. The contact angle hysteresis, that is linked to the presence of hindrances due to surface roughness or heterogeneity, for all pellets is in the range of 8–12° thus allowing to get super slippery surfaces [6].

Static contact angle values measured for all the investigated coatings are reported in Fig. 6a). It is possible to note that these values are much higher than the values reported in Fig. 5a) for the pellets made with same materials. This result indicates the importance of the coating morphology in reaching high contact angle value, i.e. low wettability, that is crucial in enhancing corrosion resistance properties since the contact time between material and environment can be greatly reduced. Highest static contact angle was assessed for the Mn-containing coating, ~ 160°, indicating the superhydrophobicity of the Mn stearate. The same can be asserted for the Zn-containing coating, whose contact angle value was ~ 152° whilst ~ 143° and ~ 98° were the contact angle values measured for Sn and Na-containing coatings, respectively. These results are in agreement with SEM micrographs shown in Fig. 4, i.e. Mn and Zn coatings have hierarchical structures whilst it is not possible to assess the same for Sn and Na coatings, with consequent higher wettability values.

For the calculation of the surface free energy (SFE, γ_{SV}) values of the

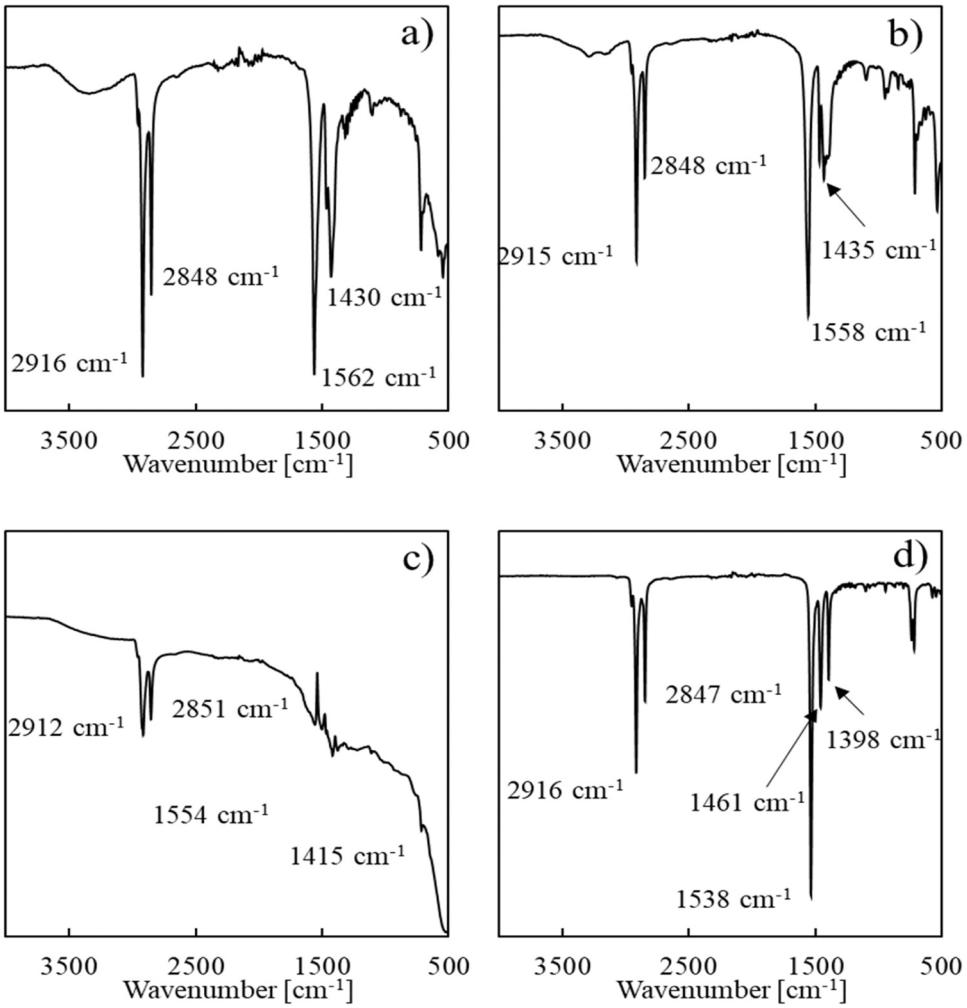

Fig. 3. FT-IR spectra of electrodeposited a) Mn coating, b) Na coating, c) Sn coating, d) Zn coating on anodized AA7075.

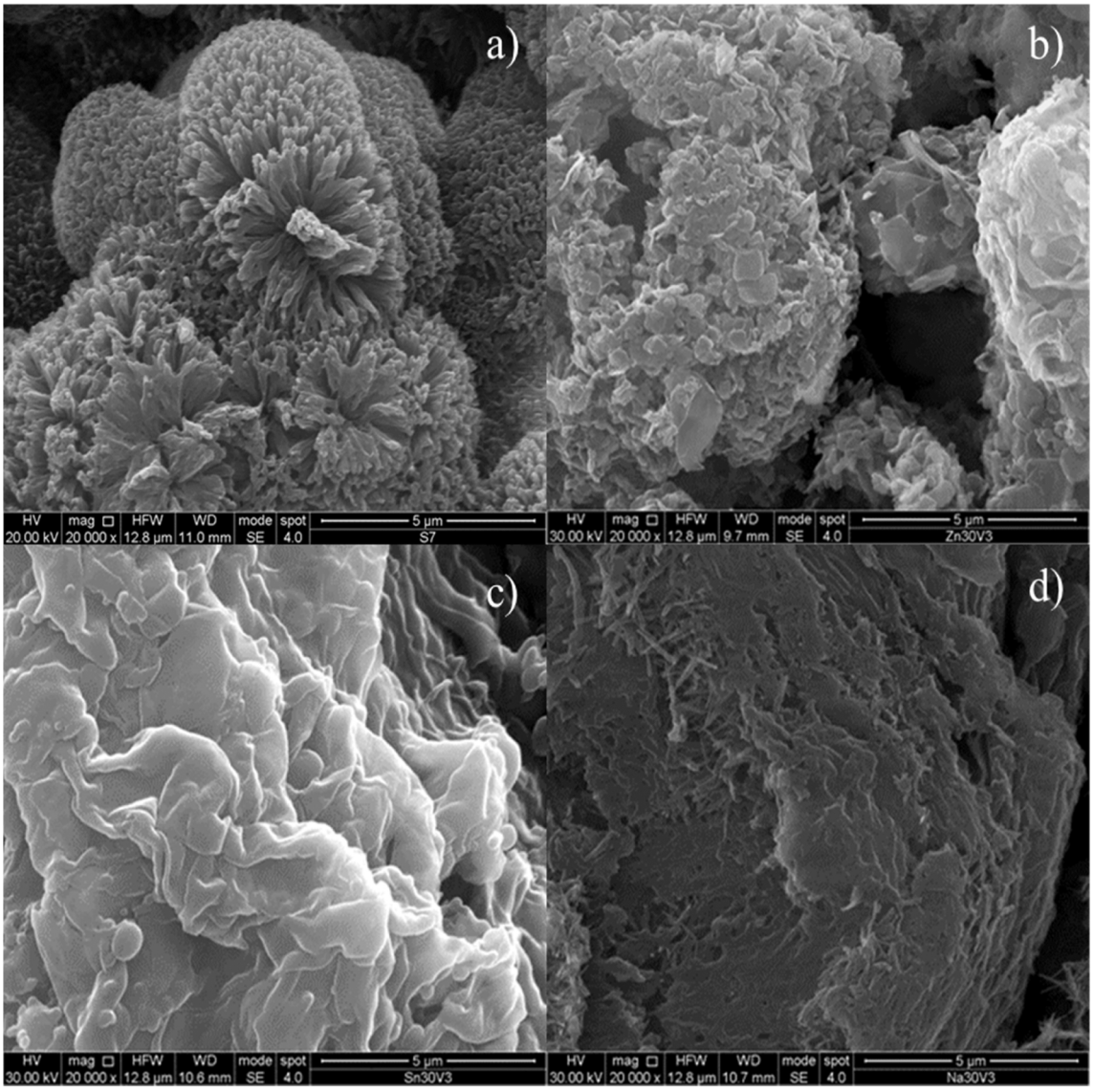

Fig. 4. SEM micrographs of electrodeposited a) Mn coating, b) Zn coating, c) Sn coating, d) Na coating on anodized AA7075.

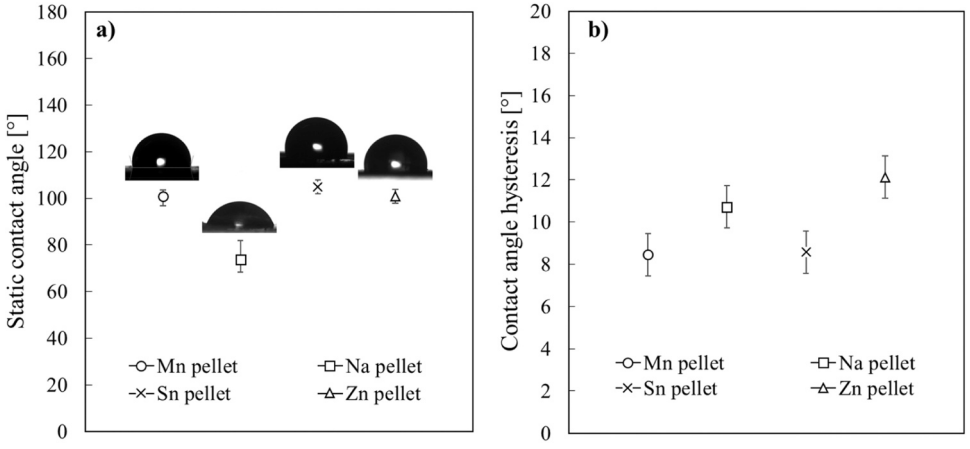

Fig. 5. Measured a) static contact angles and b) contact angle hysteresis, for pellets.

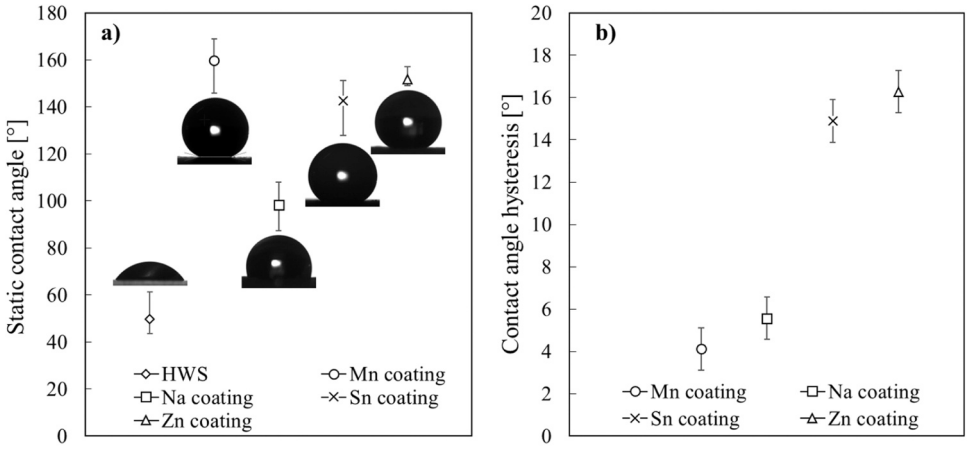

Fig. 6. Measured a) static contact angles and b) contact angle hysteresis, for electrodeposited coatings on anodized AA7075.

coatings, the OWRK method was applied. The latter requires two different liquids for the measure and the surface tension is interpreted as the sum of a dispersive component, γ^D, and a polar component, γ^P [13]. Knowing the surface tension of the two liquids (in this work water surface tension γ_{LV_W} and toluene surface tension γ_{LV_T}) (see Table 3) [17], SFE is evaluated according to the following equations:

$$\gamma_{LV_W}(1+\cos\theta_W) = 2\left[\sqrt{\left(\gamma^D_{SV}\gamma^D_{LV_W}\right)} + \sqrt{\left(\gamma^P_{SV}\gamma^P_{LV_W}\right)}\right] \quad (4)$$

$$\gamma_{LV_T}(1+\cos\theta_T) = 2\left[\sqrt{\left(\gamma^D_{SV}\gamma^D_{LV_T}\right)} + \sqrt{\left(\gamma^P_{SV}\gamma^P_{LV_T}\right)}\right] \quad (5)$$

$$\gamma_{SV} = \gamma^D_{SV} + \gamma^P_{SV} \quad (6)$$

where γ_{SV} is the SFE of the studied solid surface and θ_W and θ_T are static contact angles measured using water and toluene, respectively. Table 4 shows the angles used and the SFE values obtained for HWS samples and for the pellets.

These values are in agreement with those reported in literature for different superhydrophobic coatings on porous aluminium oxide, as those modified by polydimethylsiloxane (PDMS) [18].

In order to rationalize the significantly high static contact angle values measured for the electrodeposited coatings on anodized AA7075 samples, it is necessary to take into account the role of coating morphology. According to Cassie-Baxter theory, the contact angle on a rough surface, θ_R, is a function of the corresponding static angle on a flat surface (θ) according to the following eq. [19]:

$$\cos\theta_R = f_s(\cos\theta+1)-1 \quad (7)$$

where f_s is the fraction of the surface actually in contact with the droplet. By substituting the experimental values of the angles measured on the coatings and pellets, f_s values can be estimated (see Table 5).

For Mn and Zn, the low f_s values estimated are in agreement with the nanostructured hierarchical morphology for these coatings as shown in SEM micrographs of Fig. 4. The higher f_s values estimated for Sn and Na confirm a less pronounced or absent hierarchical structure. These findings suggest a prominent role of cauliflower morphologies in providing super hydrophobicity to the coating.

Table 3
Liquid surface tension components of Water and Toluene from ref. [17].

	γ_{LV} [mJ m^{-2}]	γ^D [mJ m^{-2}]	γ^P [mJ m^{-2}]
Water – H_2O	72.8	26.4	46.4
Toluene - TOL	28.4	26.1	2.3

Table 4
Contact angles values using water and toluene, and SFE estimates.

	Water CA [°]	Toluene CA [°]	SFE [mJ m^{-2}]
HWS	50	4.5	49.7
Mn pellet	101	33.5	24.5
Na pellet	74	22.7	31.3
Sn pellet	105	23.9	27.3
Zn pellet	101	25.8	26.7

Table 5
Fraction of the surface actually in contact with the droplet.

	f_s
Mn coating	0.07
Na coating	0.67
Sn coating	0.27
Zn coating	0.14

3.3. Corrosion resistance properties

In order to assess the corrosion resistance of the samples, EIS spectra were recorded at the open circuit potential (OCP) in 3.5 wt% NaCl solution and are shown in Fig. 7.

At a first glance it is evident a huge increase of the overall impedance for the anodized alloys after manganese stearate deposition with respect to the hot water sealed anodized alloy. A less important but still beneficial effect is also provided by zinc stearate deposition, while $CH_3(CH_2)_{16}COONa$ and $Sn[CH_3(CH_2)_{16}COO]_2$ containing coating do not enhance the overall measured impedance with respect to HWS alloys. In order to get quantitative information from the EIS spectra, the latter were fitted according to the equivalent electrical circuit (EEC) of Fig. 8.

The non ideal capacitance of the porous layer is mimicked by a constant phase element Q_P, while the impedance of the barrier layer is modelled by a parallel between R_b and Q_b accounting for its resistance and non-ideal capacitance, respectively. A CPE was inserted to model the complex structure of products inside the porous anodic oxide [12]. R_{el} is finally the resistance of the electrolyte. The fitting parameters and OCP values are reported in Table 6.

A strong shift (in the order of + 0.5 V) of the OCP is measured for the anodized samples covered by Mn stearate and Zn stearate. Conversely, the deposition of Na and Sn stearate does not affect significantly the open circuit potential with respect to anodized alloy before (see Table S1) and after hot water sealing. In the case of Mn stearate samples, it is important to note that R_b is four orders of magnitude higher than R_b for HWS samples. This can be explained by considering a good adhesion

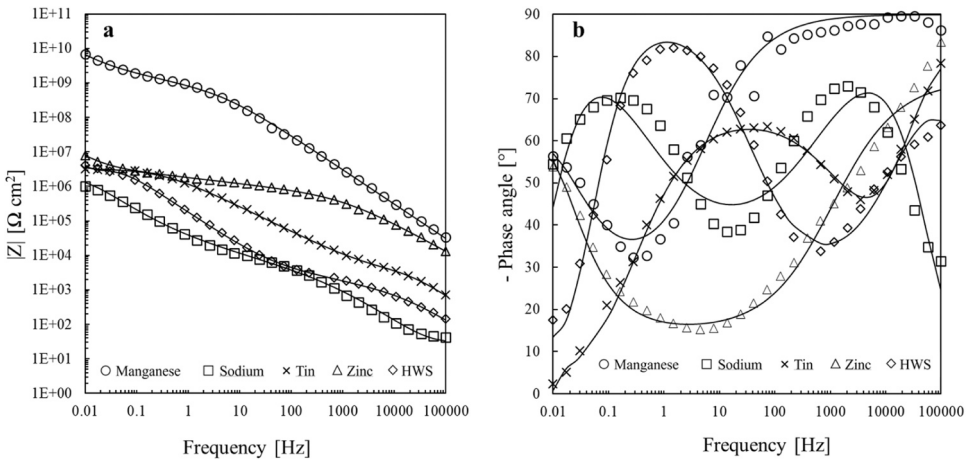

Fig. 7. Bode representation of the EIS spectra for different coatings in seawater mimicking solution. Continuous line: fitting line.

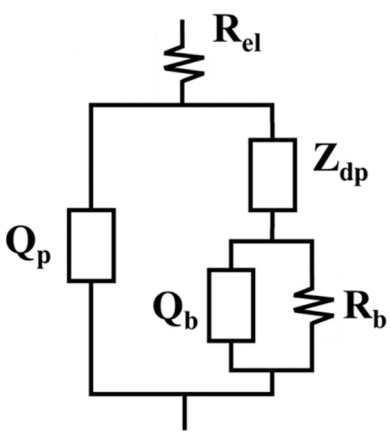

Fig. 8. Equivalent electrical circuit (EEC) model used for coated samples.

of the stearate on barrier oxide layer since during the electrodeposition process the electric field mainly drops inside the barrier layer inducing the precipitation of the stearate starting from the bottom of the pores. The good adhesion of the coating on the oxide substrate is confirmed by the Q_p and Q_b values that are lower with respect to those measured for HWS samples suggesting a thickening of the dielectric, constituted by the anodic oxide and the manganese stearate, grown by the electrodeposition process. Z_{dp} with a n of ~ 0.2 has a resistive behaviour with an impedance five order of magnitude higher than that related to HWS sample.

Zinc stearate behaviour is similar to that of Mn stearate but with lower value for R_b suggesting the formation of a thinner coating. However, this value is still one order of magnitude higher with respect to HWS, while the presence of Sn stearate does not affect R_b. Conversely, the electrodeposition of Na stearate reduces significantly the resistance of the barrier layer. It is likely that during the process Na ions are inserted into anodic alumina with consequent reduction of the Al_2O_3 resistance [20]. Highest corrosion resistance shown by Mn stearate coating was also confirmed by looking at the polarization curves recorded in the same seawater mimicking solution (see Fig. S3).

Due to its outstanding behaviour, we focused on the durability of manganese stearate coating and for comparison on HWS samples carrying out long term immersion test in 3.5 wt% NaCl solution. Figs. 9 and 10 show the EIS spectra recorded at OCP after 21 days of immersion.

A slight decrease (to ~ 10^9 Ω·cm^2) of the overall impedance for Mn stearate coated samples can be noticed, even if this impedance is much higher than the overall impedance for HWS sample after same immersion time (~10^5 Ω·cm^2) thus suggesting the success of sealing the pores of the anodic layers using manganese stearate. In Fig. 11, static contact angles as a function of immersion time in 3.5 wt% NaCl are also reported. After 21 days of immersion, static contact angle retains a value > 120° (140 ± 2°), i.e. the samples are still hydrophobic, exhibiting a high protective action in a marine-like corrosion environment, in agreement with the EIS spectra reported in Fig. 10 and with the polarization curves reported in Fig. S4.

4. Conclusions

Coatings of Na, Mn, Sn and Zn stearates were electrodeposited onto the surface of anodized AA7075 alloy in order to seal the pores of the anodic layer. Coatings were characterized, studying their superhydrophobic properties by considering their chemical and morphological structure. According to these characterizations, Mn stearate coating had a contact angle value of ~ 160° and resulted the sample with the highest corrosion resistance, thus it was also tested by immersion in sea water solution until 21 days. After this immersion, an overall impedance of ~ 10^9 Ω·cm^2 was measured, almost 3 orders of magnitude higher than the samples sealed by hot water sealing evaluated in the same conditions. Moreover, the superhydrophobic layer showed a still high static contact angle, ~ 143°, even after 21 immersion days in 3.5 wt% NaCl aqueous solution. These results show the effectiveness of the electrodeposition process in replacing the hot water sealing to obtain sealed anodic porous oxides with superhydrophobic behaviour and long-lasting

Table 6
Fitting parameters related to EIS spectra reported in Fig. 7. R_{el} = 30 Ω cm^2 for all the samples.

	Q_p [S s^n cm^{-2}]	n	Z_{dp} [S s^n cm^{-2}]	n	R_b [Ω cm^2]	Q_b [S s^n cm^{-2}]	n	χ^2	OCP [V vs SSC]
HWS	$1.1 \bullet 10^{-8}$	1	$4.6 \bullet 10^{-5}$	0.28	$3.2 \bullet 10^{6}$	$8.9 \bullet 10^{-7}$	1	$5.21 \bullet 10^{-3}$	-0.66
Mn	$5.2 \bullet 10^{-11}$	1	$6.3 \bullet 10^{-10}$	0.28	$2.7 \bullet 10^{10}$	$3.7 \bullet 10^{-9}$	1	$1.18 \bullet 10^{-2}$	0.01
Na	$1.1 \bullet 10^{-7}$	1	$1.7 \bullet 10^{-5}$	0.40	$1.6 \bullet 10^{6}$	$1.0 \bullet 10^{-5}$	1	$2.94 \bullet 10^{-2}$	-0.65
Sn	$2.2 \bullet 10^{-9}$	1	$1.2 \bullet 10^{-4}$	0.06	$3.3 \bullet 10^{6}$	$1.8 \bullet 10^{-7}$	0.73	$1.02 \bullet 10^{-3}$	-0.56
Zn	$1.1 \bullet 10^{-9}$	0.83	$4.1 \bullet 10^{-7}$	0.16	$4.0 \bullet 10^{7}$	$2.8 \bullet 10^{-6}$	1	$4.91 \bullet 10^{-3}$	-0.12

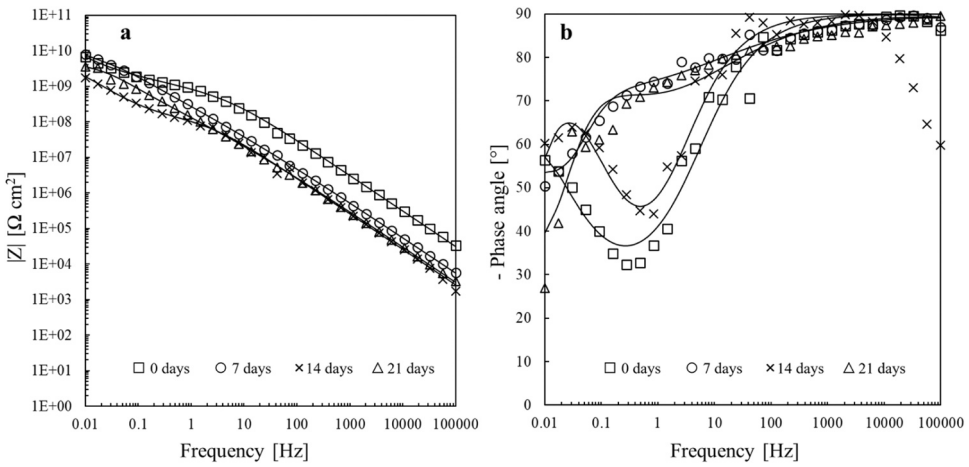

Fig. 9. Bode representation of the EIS spectra for Mn coated samples after 7, 14, 21 days of immersion in seawater-mimicking solution.

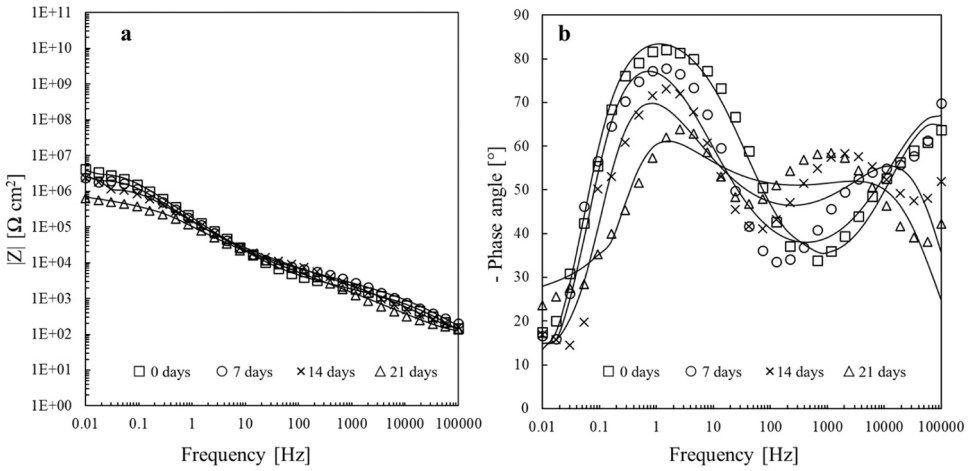

Fig. 10. Bode representation of the EIS spectra for HWS samples after 7, 14, 21 days of immersion in seawater-mimicking solution.

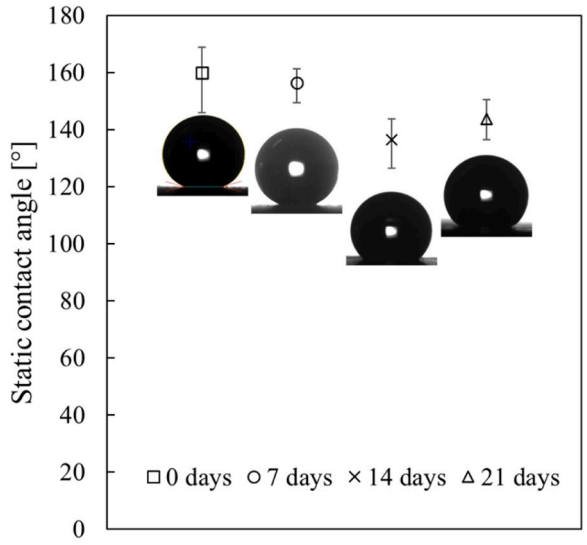

Fig. 11. Static contact angles for the Mn coated samples after 7, 14, 21 days of immersion in seawater-mimicking solution.

corrosion resistance properties.

Funding

This research did not receive any specific grant from funding agencies in the public, commercial, or not-for-profit sectors.

Declaration of Competing Interest

The authors declare that they have no known competing financial interests or personal relationships that could have appeared to influence the work reported in this paper.

Data Availability

Data will be made available on request.

Appendix A. Supporting information

Supplementary data associated with this article can be found in the online version at doi:10.1016/j.colsurfa.2023.132040.

References

[1] S. Khireche, D. Boughrara, A. Kadri, L. Hamadou, N. Benbrahim, Corrosion mechanism of Al, Al–Zn and Al–Zn–Sn alloys in 3 wt% NaCl solution, Corros. Sci. 87 (2014) 504–516, https://doi.org/10.1016/J.CORSCI.2014.07.018.

[2] J.R. Scully, T.O. Knight, R.G. Buchheit, D.E. Peebles, Electrochemical characteristics of the Al2Cu, Al3Ta and Al3Zr intermetallic phases and their relevancy to the localized corrosion of Al alloys, Corros. Sci. 35 (1993) 185–195, https://doi.org/10.1016/0010-938X(93)90148-A.
[3] L. González-Rovira, L. González-Souto, P.J. Astola, C. Bravo-Benítez, F.J. Botana, Assessment of the corrosion resistance of self-ordered anodic aluminum oxide (AAO) obtained in tartaric-sulfuric acid (TSA, Surf. Coat. Technol. 399 (2020), 126131, https://doi.org/10.1016/J.SURFCOAT.2020.126131.
[4] W. Li, Y. Zhan, S. Yu, Applications of superhydrophobic coatings in anti-icing: theory, mechanisms, impact factors, challenges and perspectives, Prog. Org. Coat. 152 (2021), 106117, https://doi.org/10.1016/J.PORGCOAT.2020.106117.
[5] T. Huhtamäki, X. Tian, J.T. Korhonen, R.H.A. Ras, Surface-wetting characterization using contact-angle measurements, Nat. Protoc. 13 (7) (2018) 1521–1538, https://doi.org/10.1038/s41596-018-0003-z.
[6] K.Y. Law, Contact angle hysteresis on smooth/flat and rough surfaces. Interpretation, mechanism, and origin, Acc. Mater. Res. 3 (2022) 1–7, https://doi.org/10.1021/accountsmr.1c00051.
[7] X. Dong, J. Meng, Y. Hu, X. Wei, X. Luan, H. Zhou, Fabrication of self-cleaning superhydrophobic surfaces with improved corrosion resistance on 6061 aluminum alloys, Micromachines Vol. 11 (Page 159) (2020) 159, https://doi.org/10.3390/MI11020159.
[8] R. Yuan, H. Liu, Y. Chen, Z. Liu, Z. Li, J. Wang, G. Jing, Y. Zhu, P. Yu, H. Wang, Design ambient-curable superhydrophobic/electroactive coating toward durable pitting corrosion resistance, Chem. Eng. J. 374 (2019) 840–851, https://doi.org/10.1016/J.CEJ.2019.05.209.
[9] J. Song, L. Huang, C. Zhao, S. Wu, H. Liu, Y. Lu, X. Deng, C.J. Carmalt, I.P. Parkin, Y. Sun, Robust superhydrophobic conical pillars from syringe needle shape to straight conical pillar shape for droplet pancake bouncing, ACS Appl. Mater. Interfaces 11 (2019) 45345–45353, https://doi.org/10.1021/acsami.9b16509.
[10] F. Arianpour, S. Farhadi, M. Farzaneh, Effect of heterogeneity on hydro/ice-phobic properties of alkylsilane/fluoro-alkylsilane-based coatings on Al substrates, J. Coat. Technol. Res. 14 (2017) 267–275, https://doi.org/10.1007/s11998-016-9819-z.
[11] C. Liu, F. Su, J. Liang, Facile fabrication of a robust and corrosion resistant superhydrophobic aluminum alloy surface by a novel method, RSC Adv. 4 (2014) 55556–55564, https://doi.org/10.1039/C4RA09390A.
[12] F. Di Franco, A. Zaffora, P. Vassallo, M. Santamaria, Double step electrochemical process for the deposition of superhydrophobic coatings for enhanced corrosion resistance, J. Electrochem Soc. 168 (2021), 101502, https://doi.org/10.1149/1945-7111/AC29DF.
[13] M. Żenkiewicz, Methods for the calculation of surface free energy of solids, J. Achiev. Mater. Manuf. Eng. 24 (2007). ⟨https://www.researchgate.net/publication/40804787_Methods_for_the_calculation_of_surface_free_energy_of_solids⟩.
[14] M. Curioni, M. Saenz de Miera, P. Skeldon, G.E. Thompson, J. Ferguson, Macroscopic and local filming behavior of AA2024 T3 aluminum alloy during anodizing in sulfuric acid electrolyte, J. Electrochem Soc. 155 (2008) C387, https://doi.org/10.1149/1.2931522.
[15] O. Aras, E. Baydir, B. Akman, Highly durable spray-coated superhydrophobic surface: pre-anodizing and fatty acid chain length effect, Korean J. Chem. Eng. 39 (2022) 775–784, https://doi.org/10.1007/S11814-021-0953-7.
[16] B. Zhang, J. Li, X. Zhao, X. Hu, L. Yang, N. Wang, Y. Li, B. Hou, Biomimetic one step fabrication of manganese stearate superhydrophobic surface as an efficient barrier against marine corrosion and Chlorella vulgaris-induced biofouling, Chem. Eng. J. 306 (2016) 441–451, https://doi.org/10.1016/J.CEJ.2016.07.062.
[17] J.J. Jasper, The surface tension of pure liquid compounds, J. Phys. Chem. Ref. Data 1 (2009) 841, https://doi.org/10.1063/1.3253106.
[18] K. Olkowicz, Z. Buczko, B. Nasiłowska, K. Kowalczyk, J. Czwartos, Superhydrophobic coating based on porous aluminum oxide modified by polydimethylsiloxane (PDMS), Materials 15 (2022) 1042, https://doi.org/10.3390/MA15031042.
[19] A. Kavitha Sri, P. Deeksha, G. Deepika, J. Nishanthini, G.S. Hikku, S. Antinate Shilpa, K. Jeyasubramanian, R. Murugesan, Super-hydrophobicity: mechanism, fabrication and its application in medical implants to prevent biomaterial associated infections, J. Ind. Eng. Chem. 92 (2020) 1–17, https://doi.org/10.1016/j.jiec.2020.08.008.
[20] S.C. Jung, H.J. Kim, J.W. Choi, Y.K. Han, Sodium ion diffusion in Al2O3: a distinct perspective compared with lithium ion diffusion, Nano Lett. 14 (2014) 6559–6563, https://doi.org/10.1021/NL503169V.